Structural and Control Concepts for Variable Geometry Planetary Entry Systems

Marco Quadrelli[1], Dhemetrios Boussalis[2], Gregory Davis[3]
Jet Propulsion Laboratory, California Institute of Technology, Pasadena, CA 91109
and
Kawai Kwok[4], Sergio Pellegrino[5]
California Institute of Technology, Pasadena, CA 91125

The results presented in this paper apply to a generic vehicle that makes use of geometry changes to modulate the heat, drag, and acceleration loads while entering a planetary atmosphere. Two structural concepts for implementing the cone angle variation, namely a segmented shell and a corrugated shell, are presented. A structural analysis of the corrugated shell configuration shows that the stress levels are tolerable during entry. The analytic expressions of the longitudinal aerodynamic coefficients are also derived, and guidance laws that track reference heat flux, drag, and aerodynamic acceleration loads are also proposed. These guidance laws have been tested in an integrated simulation environment, and the results indicate that use of variable geometry is feasible to track specific profiles of dynamic load conditions during reentry.

Nomenclature

B = Bluntness Ratio
C_A = Axial Force Coefficient
C_D = Drag Coefficient
C_L = Lift Coefficient
C_N = Normal Force Coefficient
C_Y = Side Force Coefficient
Cm = Pitching Moment Coefficient
d = Meridian Length
h = Altitude
L/D = Lift-to-Drag Ratio
m = Mass
R = Reference Radius
r_n = Nose Radius
R_p = Planet Radius
L = Axial Length
S = Reference Area
V_∞ = Free-stream Dynamic Pressure
X_{CP} = Center of Pressure
α = Angle of Attack
β = Sideslip Angle
β_m = Ballistic Coefficient
γ = Flight Path Angle
δ = Cone Angle

---

[1] Senior Engineer, Mail Stop 198-326, Guidance and Control Analysis Group, 4800 Oak Grove Drive, Marco.B.Quadrelli@jpl.nasa.gov
[2] Senior Engineer, Dhemetrio.Boussalis@jpl.nasa.gov
[3] Principal Engineer, Mail Stop 125- 220A, , Gregory.L.Davis@jpl.nasa.gov
[4] Graduate Student, Graduate Aeronautical Laboratories, 1200 E. California Blvd. MC 301-46, kwk5@caltech.edu
[5] Professor of Aeronautics and Civil Engineering, Graduate Aeronautical Laboratories, 1200 E. California Blvd. MC 301-46, AIAA Fellow. sergiop@caltech.edu

I. Introduction

This paper presents the results of study of the effect of variable aerodynamic coefficients on the structural dynamics and trajectory of a vehicle entering a planetary atmosphere. Some of the key challenges of planetary entry are to dissipate the large kinetic energy of the entry vehicle and to land with precision. Past missions to Mars were based on unguided entry, where entry vehicles carried payloads of less than 0.6 T and landed within 100 km of the designated target. The Mars Science Laboratory (MSL) is expected to carry a mass of almost 1 T to within 20 km of the target site[1]. Guided lifting entry is needed to meet these higher deceleration and targeting demands. Decelerators in prior missions to Mars were based on 70 degree sphere-cone geometry, as shown in Figure 1. To produce lift with such an axi-symmetric vehicle, the present approach is to trim at a nonzero angle of attack by center-of-mass (c.o.m.) offset through most of the hypersonic entry phase. The resulting trajectory is dependent on the lift-to-drag ratio L/D and ballistic coefficient β_m inherent in the decelerator. If the aerodynamic characteristics of the decelerator is variable during flight, more trajectory options are possible, and can be tailored to specific mission requirements. In addition to the entry trajectory modulation, having variable aerodynamic properties will also favor maneuvering of the vehicle prior to descent. For proper supersonic parachute deployment, the vehicle needs to turn to a lower angle of attack. Currently, MSL relies on expelling ballast masses of 100 kg, 10% of its landed mass, in making a pitch maneuver to reduce the angle of attack.[2] Such maneuvers cannot be repeated during flight without added mass penalties. For maneuvering entry vehicles with blunt sphere-cone geometry, one common approach is to trim the vehicle at a nonzero angle of attack to produce lift by center-of-mass offset through most of the hypersonic entry phase. However, the vehicle needs to turn to a lower angle of attack prior to supersonic parachute deployment. One approach to entry trajectory improvement and angle of attack control is to embed a variable geometry decelerator in the design of the vehicle. Variation in geometry enables the vehicle to adjust its aerodynamic performance continuously without additional fuel cost because only electric power is needed for actuating the mechanisms that control the shape change. Novel structural and control concepts that enable the decelerator to undergo variation in geometry are the subject of this paper. It should be noted that other alternatives that have been proposed for the aerodynamic control problem make use of aerodynamic surfaces such as tabs or flaps[3]. They are either fixed in configuration or single- shot deployable, which limits them to only a few discrete configurations. In contrast, a variable geometry decelerator offers a continuous variation in vehicle configurations and aerodynamic performance.

Changing the aerodynamic characteristics of a flight vehicle by active means can potentially provide a mechanically simple, affordable, and enabling solution for entry, descent, and landing across a wide range of mission types, sample capture and return, and reentry to Earth, Titan, Venus, or Mars. Unguided ballistic entry is not sufficient to meet this more stringent deceleration, heating and targeting demands. Active guidance is needed and this requires more general aerodynamic control capabilities in the entry vehicles. We consider a vehicle with a forebody that is expanded to increase drag at high altitudes and high speeds, and that can be contracted at lower altitudes and speeds to decrease drag. In this manner, the deceleration curve as a function of time is flattened out so that the maximum deceleration is reduced. Reductions of drag up to 20% appear possible: a rough calculation shows that for a vehicle entering the Martian atmosphere, a 20% change of drag area, modulated by a variable geometry change in the 20-55 km altitude range, results in a 16% reduction of the maximum temperature peak, a 3% reduction in peak acceleration, and a 10% L/D change, making a significant difference in enabling lateral maneuverability during descent. This increased performance is achieved at no fuel cost: only electric power is used to actuate the motors driving the kinematical linkage of the underlying adaptive skeleton structure and can take place in very short time, typically before the peak heat rate or peak deceleration occur.

This paper is organized as follows. Section II describes the entry dynamics and aeroheating during entry trajectory. Section III presents an analysis on the effect of geometric variation on the aerodynamic performance of decelerator. Section IV proposes the structural concepts for geometric variation that have been studied. Section V presents a structural performance analysis of the proposed corrugated shell concept. Section VI derives guidance laws for trajectory modulation. Section VII demonstrates the trajectory simulation results with tunable aerodynamic coefficients. Section VIII concludes the paper and outlines the future work for this study.

American Institute of Aeronautics and Astronautics

Figure 1. 70 degree MSL sphere-cone aeroshell (representative low L/D geometry studied in this paper).

II. Dynamic Modeling

For precision landing with specified deceleration requirements, trajectory modulation needs to start early in the hypersonic segment of the reentry. In this section, the assumptions and equations of motion of the vehicle dynamics and thermodynamics entering a planetary atmosphere are derived. Some proposed guidance laws based on dynamic inversion are also discussed, as well as preliminary results of simulation studies.

A. Longitudinal Vehicle Dynamics

The dynamic performance of the entry vehicle is examined in this section. Our analysis follows the following assumptions[4,11]:
- The vehicle is rigid and axially symmetric, but of varying geometry;
- The vehicle exhibits only small perturbations about a nominal flight condition, so that the motion of the vehicle can be decoupled into longitudinal (in the plane of symmetry) and lateral (out of plane) motions. The perturbations and symmetric flight assumptions are valid for a wide range of flight conditions. They are violated only in large amplitude maneuvers such as rapid rolls, tight turns, and rolling pull-outs, i.e. maneuvers expected of high performance aircraft but rather unlikely to be encountered in precision landing applications.
- motion restricted to the longitudinal plane (i.e., side-slip angle=0);
- the planet is spherical and rotating at constant rate.
- The atmosphere density is modeled by an exponential model of the form $\rho = \rho_0 \exp(-\beta_a h)$, where ρ_0 is the reference density and β_a the scale height.

Under these assumptions, the kinematic equations of longitudinal planar motion for generic atmospheric reentry of a capsule can be expressed as follows[16,17]:

$$
\begin{aligned}
\dot{h} &= V \sin\gamma \\
\dot{\theta} &= \frac{V \cos\gamma \cos\psi}{r \cos\phi} \\
\dot{\phi} &= \frac{V \cos\gamma \sin\psi}{r} \\
\dot{\alpha} &= q + \dot{\gamma} + \dot{\phi}\sin\psi + (\Omega + \dot{\theta})\cos\psi
\end{aligned}
\tag{1}
$$

while the dynamic equations are

$$\dot{V} = -\frac{D}{m} - g\sin\gamma + C_V$$

$$\dot{\gamma} = \frac{L\cos\sigma}{mV} - \frac{1}{V}\left(g - \frac{V^2}{r}\right)\cos\gamma + C_\gamma \qquad (2)$$

$$\dot{\psi} = \frac{L\sin\sigma}{mV\cos\gamma} - \frac{V}{r}\cos\gamma\cos\psi\tan\phi + C_\psi$$

$$\dot{q} = M/I_y$$

where h is the altitude, θ the longitude angle, ϕ the latitude angle, α the angle of attack, V the magnitude of the velocity vector, γ the flight path angle, ψ the heading angle, σ the bank angle, r the vehicle distance from the center of the planet, Ω the planet rotation rate, D and L are the drag and lift forces, m the vehicle mass, g the gravitational acceleration, q is the pitch rate, I_y the pitch moment of inertia, M the pitching moment, and the C-terms represent the effect of the planet's rotation on the respective degrees of freedom. We also make use of $\beta_m = m/C_D S$, the ballistic coefficient. A smaller ballistic coefficient indicates a higher deceleration by drag on the body. Dispersions in atmospheric density and drag coefficient can impose a large variation in the altitude for parachute deployment. The ballistic coefficient can be actively controlled during the hypersonic flight so that the entry vehicle will reach the required velocity at descent stage.

B. Thermal Dynamics

Stagnation point heating approximation methods can then be used to estimate the convective and radiative heat rates of a vehicle that follows a given atmospheric trajectory. For a vehicle entering a planetary atmosphere, the time rate of change of average convective heat input per unit area at the stagnation point can be estimated with the general expression:

$$\dot{Q}_{in} = c_1 \rho^{\frac{1}{2}} V^n \qquad (3)$$

where c_1 is a constant and the exponent n is between 3 and 3.5. In this paper, we assumed n=3 for reference. The convective heat flux at stagnation point near the nose of radius R_{nose} can also be expressed as:

$$\dot{Q}_{in} = 0.0145\sqrt{2000.0\frac{q_{dyn}}{R_{nose}}}V^2 \qquad (4)$$

The Reynolds number is $\mathrm{Re} = \dfrac{\rho \bar{c} V}{\nu}$, where $\nu\nu$ is the viscosity, and the skin friction coefficient Cf can be written as $Cf_{laminar}$=0.664/sqrt(Re) if Re<2300, or $Cf_{turbulent}$=0.0592/(Re^0.2) if Re>=2300. The radiative heat flux is

$$\dot{Q}_{ex} = 4\pi S_c \varepsilon \kappa \theta^4 \qquad (5)$$

where ε is the emissivity=0.8, and κ is the Boltzmann constant = 5.67e-8 W/(m^{2}K^4). The thermal balance at the stagnation point can then be written as:

$$\dot{\theta} = \frac{\dot{Q}_{in} - \dot{Q}_{ex}}{m\rho_m c_p} \qquad (6)$$

where m is the vehicle mass, ρ_m=7.8e3 is the material density in kg/m3, and c_p=5.68 is the material specific heat at constant pressure.

III. Aerodynamic Characteristics of Sphere-Cone with Variable Cone Angle

The dependence of the vehicle's deceleration on the ballistic coefficient $\beta_m = \dfrac{m}{C_D S}$ can be seen in Eq. (2). A smaller ballistic coefficient indicates a higher deceleration by drag on the body. The entry range dispersion is sensitive to the initial error in flight path angle at the entry interface. The rate of change of flight path angle is proportional to the lift-to-drag ratio (L/D), which can be designed to minimize the range dispersion. For example, for MSL, a minimum L/D of 0.25 is required for a landing precision of 10 km. A higher L/D would further reduce the dispersion. It would also make it possible to negotiate uncertain wind conditions and survey multiple landing zones with suitable autonomous control. For an axi-symmetric entry body, the L/D can be enhanced by flying at a higher trim angle of attack, but it is limited by the maximum required for parachute deployment requirement. One approach to this problem is to make a pitch maneuver by ejecting six identical masses. There are several alternative concepts that make use of trim-flap, tab, and shelf to fly at the required L/D at a low angle of attack. The variable geometry decelerator provides an alternative solution for L/D and bank modulation.

Entry vehicles that have flown to date feature aero-shells with blunt sphere-cone geometry, with cone angles ranging from 45 deg to 70 deg. Hence, a reasonable approach is to try to span all or part of this range in a single vehicle able to vary the cone angle of a sphere-cone shape to achieve a range of aerodynamic forces and moments during flight. For instance, given a sphere-cone with constant meridian length, an increase in the cone angle raises both the drag coefficient and the base area, which in turn reduces the ballistic coefficient of the decelerator. As will be illustrated in the following, the proposed concept enables the vehicle to vary its aerodynamic performance in a repeated manner and hence provides a means for trajectory tailoring. Possibilities of varying the geometry to change the L/D ratio include: a) Extrusion of nose section (σ); b) Flaring (opening/closing) of aft section (δ); c) Simultaneous combination of the above. This is shown in Figure 2, top. The possibilities of varying the geometry to change the L/D ratio for a biconic vehicle include: a) Extrusion of nose section (σ); b) Extrusion of middle section; c) Extrusion (expansion) of aft section; d) Flaring (opening/closing) of aft section (δ); e) Simultaneous combination of the above. This is shown in the bottom part of Figure 2.
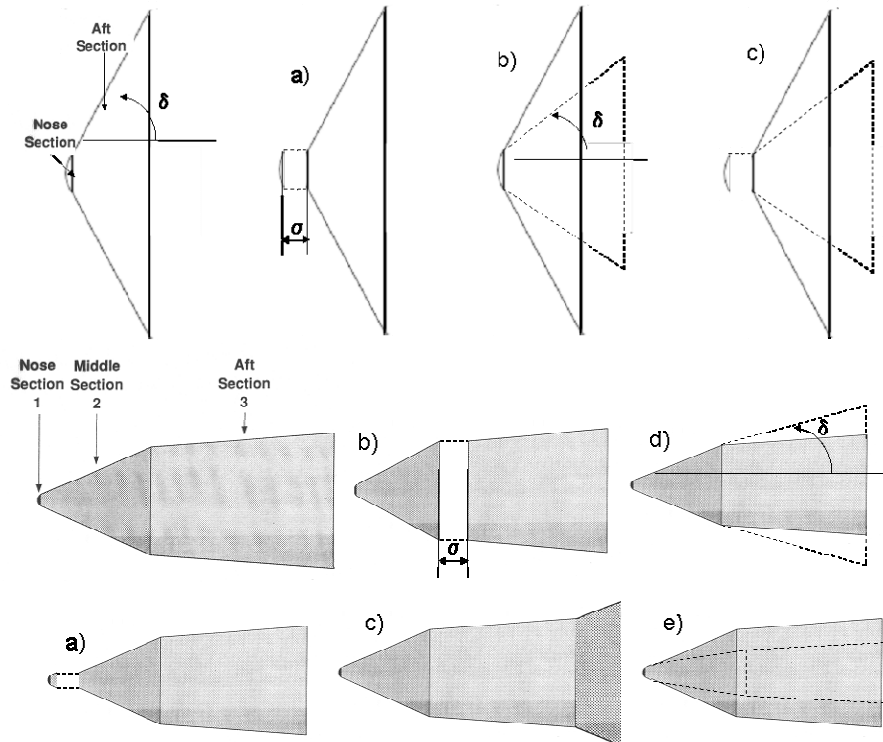

Figure 2. Possibilities of varying the geometry of a low L/D/ vehicle (top) and of a biconic vehicle (bottom).
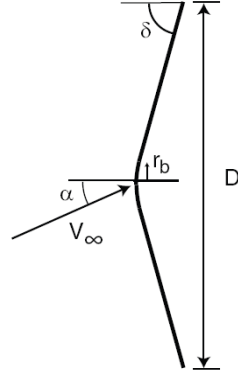
American Institute of Aeronautics and Astronautics

Figure 3. Geometry of sphere-cone and parameter definitions.

A. Continuum-Flow Aerodynamic Coefficients

In the continuum regime, hypersonic aerodynamic coefficients can be estimated using Newtonian impact theory. The Newtonian model neglects viscosity of the flow and yields a simple relation between the pressure coefficient on an elemental area and the inclination θ of the area to the free-stream. The pressure coefficient based on Newtonian flow theory depends on the relative orientation of the surface with the free-stream velocity, and is given by[5]:

$$C_p = 2\left(\frac{V_\infty}{|V_\infty|} \cdot n\right)^2 \tag{7}$$

The expression of the pressure coefficient allows for explicit integration over the surface for simple geometries, such as the sphere-cone shown in Figure 3. For the conical part of the sphere-cone, the inclination angle θ is identical to the cone angle δ. Assuming the angle of attack and sideslip angle never exceed the cone angle of the sphere-cone, there will be no shadow region. Defining the bluntness ratio as $B = \frac{r_b}{R}$, the aerodynamic force coefficients for the cone in the body reference frame are given as follows:

$$C_A = \cos^2\delta + 2\cos^2\alpha\cos^2\beta - 3\cos^2\alpha\cos^2\beta\cos^2\delta + B^2\left(-\frac{1}{2}\cos^2\delta + \frac{3}{2}\cos^2\alpha\cos^2\beta\cos^2\delta\right)$$

$$C_Y = \left(1 - \frac{1}{2}B^2\right)\cos\alpha\sin 2\beta\cos^2\delta$$

$$C_N = \left(1 - \frac{1}{2}B^2\right)\sin 2\alpha\cos^2\beta\cos^2\delta$$

$$X_{CP} = \frac{1}{\cos^2\delta\left(1 - \frac{1}{2}B^2\right)}\left[\frac{1}{3}F(\delta) - \frac{1}{2}G(\delta)\right]$$

$$F(\delta) = \tan^2\delta\left[\cot^3\delta - B^3\left(\frac{2}{\sin 2\delta} - \tan\delta\right)^3\right]$$

$$G(\delta) = \tan\delta\left[B\cot^2\delta - B^3\left(\frac{2}{\sin 2\delta} - \tan\delta\right)^2\right]$$

<div align="center">(8)</div>

The drag and lift coefficients are related to the axial and normal coefficients by a transformation from the body axis frame to the wind axis frame, and they can be derived for different angles of attack and side-slip angles. A radial c.o.m. offset is needed to provide a sufficient L/D for effective maneuvering by trimming the vehicle at a nonzero angle of attack. The MSL baseline configuration, which is a 70 deg sphere-cone, achieves the minimum L/D = 0.25 using a radial c.o.m. offset of 0.024, normalized by the maximum vehicle diameter[4]. Using this offset, the longitudinal aerodynamic coefficients of sphere-cones as a function of angle of attack for various cone angles are shown in Figure 4. At a given angle of attack, as the cone angle increases the axial force coefficient C_A increases while the normal force coefficient C_N decreases. The overall effect of varying the cone angle is to change the trim angle of attack.

B. Effect of Cone Angle on Lift-to-Drag Ratio and Ballistic Coefficient

The variations of L/D and β_m are shown in Figure 5. Aerodynamic performance is a function of the angle of attack, therefore a range of L/D and β_m are achieved by varying the cone angle. For design purposes, it is more instructive to determine the aerodynamic performance at trim conditions. Since the geometry is varying, the center of pressure, X_{CP}, moves as the decelerator changes its cone angle. The axial position and radial offset of the vehicle c.o.m. have an effect on the trim angles of attack and the corresponding L/D and β_m. Figure 6 shows the values of α, L/D, and β_m at trim conditions as functions of the cone angle for several values of the radial c.o.m. offset with a constant axial c.o.m. location. As the radial c.o.m. offset increases, both L/D and β_m decrease for the same cone angle. There is a trade off between the desired ranges of L/D and β_m when changing the radial c.o.m. offset. The optimum performance is achieved in the cone angle range of 65 deg to 75 deg, where L/D is high and β_m is small. Several alternatives to ballast masses for angle of attack control make use of aerodynamic surfaces such as tabs or flaps. They are either fixed in configuration or single-shot deployable, which limits them to only a few discrete configurations. In contrast, a variable geometry decelerator offers a continuous variation in vehicle configurations and aerodynamic performance.
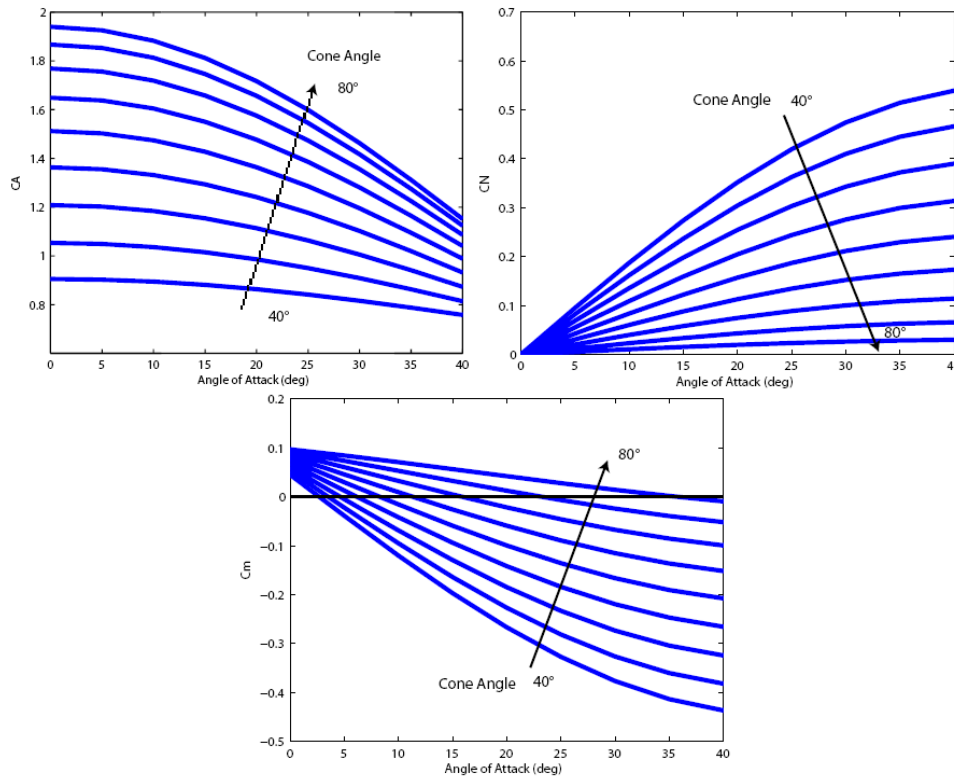

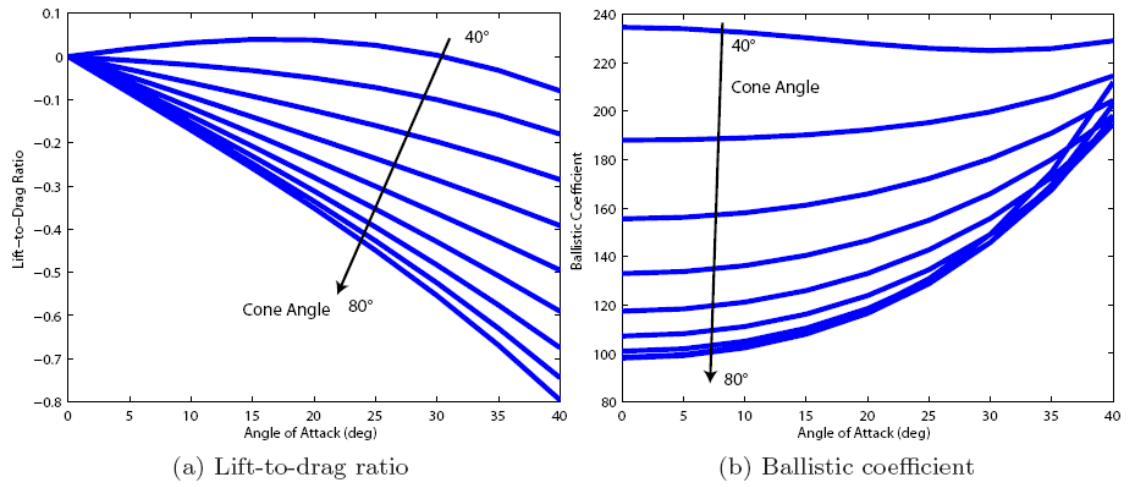**Figure 4. Effect of cone angle on longitudinal aerodynamic coefficients.**

(a) Lift-to-drag ratio (b) Ballistic coefficient

Figure 5. Variation of ballistic coefficients and L/D ratio for various cone angles.
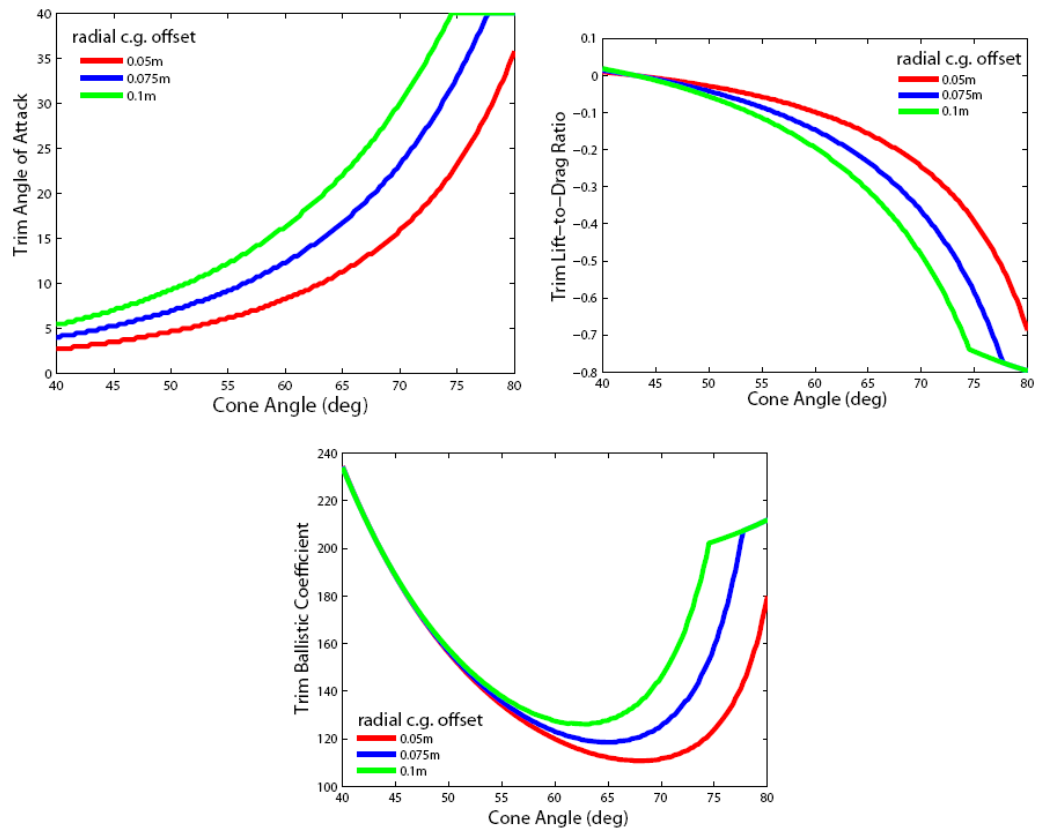

Figure 6. Trim aerodynamic parameters vs. cone angle.

IV. Structural Control Concepts

Two structural concepts for variable geometry decelerators are presented. The first concept envisages a segmented thin shell structure whose component parts are hinged to a rigid nose element and are supported by a hoop of variable radius near the outer rim. The second concept envisages a flexible shell structure which changes configuration in response to a radius change imposed by, for example, a set of actuators. An important component of both of these decelerator concepts, which will not be discussed in detail, is a thermal protection system (TPS) that reduces the thermal load on the structure itself. To achieve a smooth variation in the geometric configuration of the decelerator with a high degree of control on the decelerator shape requires that the behavior of the TPS be considered as well. The segmented shell decelerator concept requires the TPS to bridge across the gaps between the segments, whereas the flexible shell concept requires the TPS to change curvature. In both cases it is important to consider the stiffness properties of currently available TPS materials in the design process. The TPS for MSL consists of cork-filled silicone bonded onto a Flexcore honeycomb; it has a thickness of about 25 mm [6]. It is likely to be too stiff for the proposed concepts and the maximum strain that it can survive without fracturing would have to be evaluated to determine the limits on the underlying surface movements that could be tolerated. An alternative approach that is believed to be more suitable for the proposed schemes is based on recent developments in inflatable entry vehicles, which feature a flexible high temperature multilayer insulation (MLI) consisting of ceramic, carbon fabric, metal foil, and metalized Kapton layers. It has been experimentally demonstrated that a MLI with 25 layers and a total thickness of 4.29 mm is able to keep the temperature of the bottom layer below 200°C under a heat flux of 35 W/cm^2.[7] Since MLI is composed of distinct thin layers, its bending stiffness can be assumed to be small in comparison with the stiffness of the underlying shell structure and hence can be neglected in a preliminary study.

A. Segmented Shell

The segmented shell concept is based on a continuous spherical blunt nose and a number of curved panels that are sections of a conical surface. Each of the curved panels is connected to the nose by a hinge and the variation in cone angle is achieved by rotating the curved panels about the nose. Such rotation is carried out by controlling the base radius of the structure. This is a mechanism-type concept, see Figure 7, which involves no deformation of the surfaces and is thus compatible with conventional ablative materials, such as the MSL TPS, but would require the use of a compliant MLI to span across the panels.

A kinematic simulation of the segmented shell concept has shown that the clearance between adjacent panels, required for expansion and retraction without interference, is the limiting factor for the variable cone angle range. Figure 8 shows the retracted and expanded states of a prototype that provides a cone angle range of 15 deg. In the model shown in Figure 8, the gaps between adjacent conical segments have been minimized by allowing the panels to overlap in the retracted configuration, to support the MLI that would then seal off. There would be, of course, discontinuities in the curvature of the surface which are expected to have adverse effects on the heat load distribution on the entry vehicle. A second concept has been proposed that provides a continuous surface and is presented in the next section.
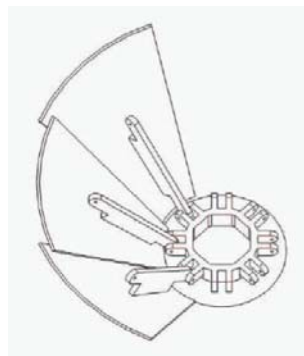

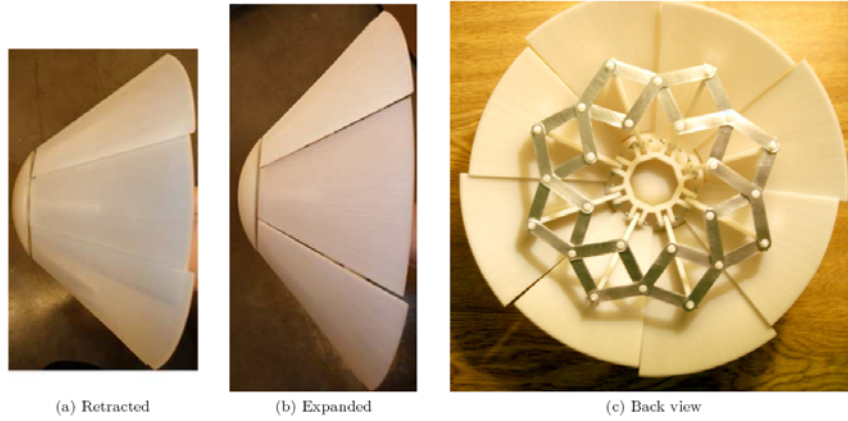**Figure 7. Geometry of segmented shell showing 3 panels and nose element.**

(a) Retracted   (b) Expanded   (c) Back view

Figure 8. Geometry variation of segmented shell model consisting of 8 panels plus nose element.

B. Corrugated Shell

The idea is to design a thin shell structure of essentially conical shape whose angle can be varied over a useful range without stretching the surface. Hence, the shell has to bend only and this generally requires a smaller amount of strain energy than a comparable geometry change involving stretching of the surface. A range of purely conical surfaces can be inextensionally transformed into one another by varying the directrix in such a way that its arc length remains unchanged and the distance between the apex of the cone and any point of the directrix is also unchanged. Hence, a smooth cone (with a circular directrix) can be transformed into a corrugated cone with a non-planar directrix and a smaller (average) cone angle. Alternatively, the average cone angle of an initially corrugated cone can be either increased by decreasing the amplitude of the corrugation, or decreased by increasing this amplitude.

This concept is illustrated in Fig. 9 which depicts a corrugated conical surface that has been obtained by stitching a smooth spherical cap, to provide the blunt nose region, to a truncated conical surface with corrugations in the form of a sine function. As shown in Fig. 10a, the corrugated conical surface is a ruled surface bounded by two curves, DEF and PQR, which respectively lie on spheres of two different radii, r_0 and r_h, centered at O. The curve DEF is not corrugated to allow a continuous connection between the corrugated conical surface and a sphere cap, as shown in Fig. 10b. Any curve obtained by intersecting the corrugated conical surface with a sphere centered at O and with a radius between r_0 and r_h is described by

$$\theta = \delta_0 + A\left(1 - \frac{r_0}{r}\right)\cos(n\phi) \quad \text{with } \phi \in [0, 2\pi], \ r \in [r_0, r_h] \tag{9}$$

where δ_0 is the average cone angle in radians, n is the number of corrugations, and A is the corrugation amplitude in radians. Because of the corrugations the cone angle varies between two limits; but a single value, obtained by averaging over the cross section, will be used for describing the geometry of the corrugated cone. Similarly, the outer rim radius of the corrugated shell is also an average value.

A small scale physical model of this concept, with a diameter of 300 mm, a thickness of 1 mm, an undeformed average cone angle δ_0 = 60 deg (1.05 rad) and a corrugation amplitude A = 3.10 deg (0.054 rad) has been analyzed using the commercial software package ABAQUS[8]. The peak stresses resulting from the geometry change and the associated reaction forces were predicted by the finite element simulation to ensure that they would be compatible with the stereolitography material Somos 9920 that has a Young's modulus of 1580 MPa and a breaking strain of 21%[9]. The model was fabricated after confirming that its deformation would be entirely elastic. The photos in Fig. 11 show the corrugated shell in the two extreme configurations, with average cone angles of 65 deg and 55 deg when expanded and retracted, respectively.
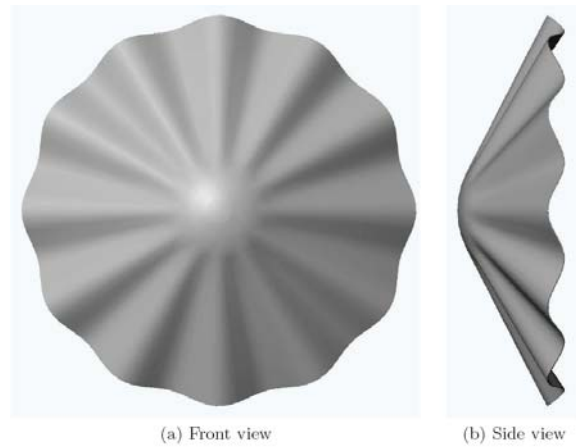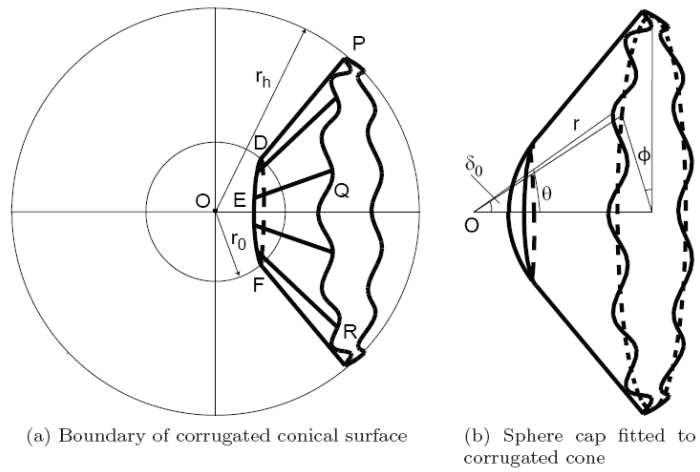
American Institute of Aeronautics and Astronautics

(a) Front view   (b) Side view

Figure 9. CAD model of corrugated shell.

(a) Boundary of corrugated conical surface   (b) Sphere cap fitted to corrugated cone

Figure 10. Geometry of corrugated shell.

American Institute of Aeronautics and Astronautics
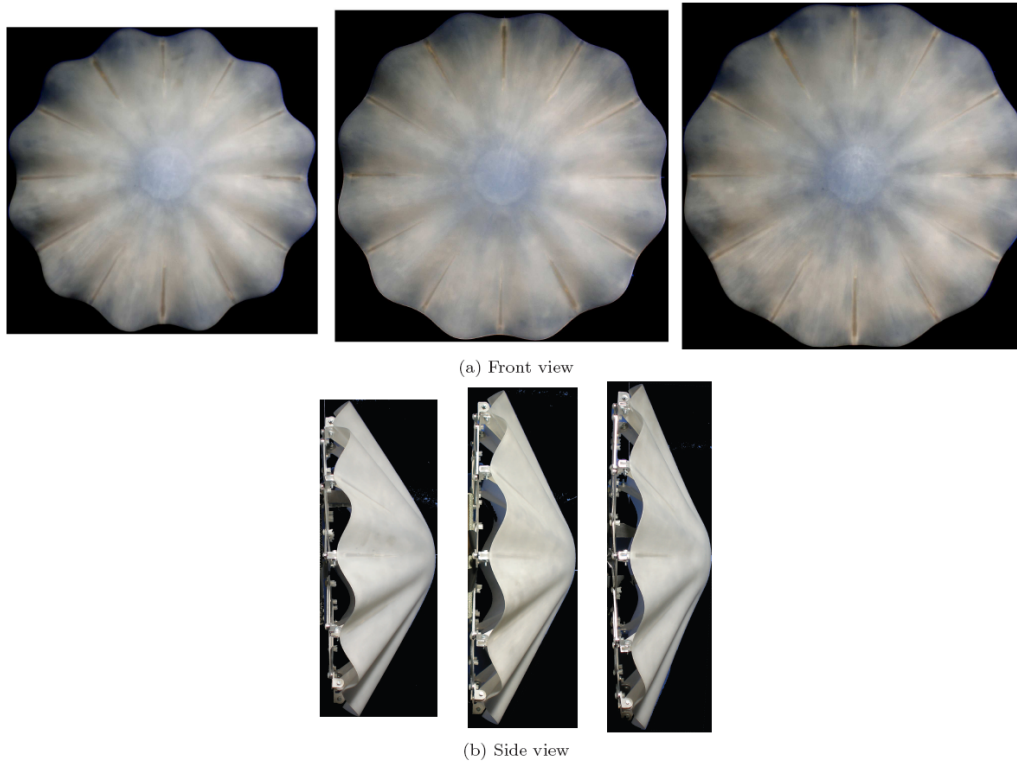
(a) Front view

(b) Side view

Figure 11. Geometry variation of corrugated shell model.

C. Actuation Scheme

The shape variation is actuated by changing the radius at the rear of the decelerator by means of an actuation mechanism. In the case of the proof-of-concept prototypes presented in this paper, the radial motion of the base has been achieved through a circular foldable bar structure with mobility of one.[10] This single internal degree of freedom allows the structure to keep all of the outer joints on a circle of uniform radius, varying in a given range. This mechanism is formed by connecting identical angulated bars using shear connectors. Figure 12 shows the retracted and expanded configuration of a circular foldable bar structure consisting of eight pairs of angulated elements. The connection points on the outer circumference of the mechanism are attached to the base of the prototypes. This bar structure is proposed only for small scale prototypes as it is expected that in a full scale decelerator several linear actuators would be utilized to provide higher forces and to achieve both symmetric and asymmetric configuration changes.

V. Analysis of Full-Scale Corrugated Shell Concept

Having established that cone angle variations in a range compatible with the aerodynamic studies in Section III are achievable with the corrugated shell concept for the scale of a scaled prototype, a full-scale decelerator employing this concept has been designed and analyzed for its structural performance. A finite element model of this structure has been set up in ABAQUS[8] to study the static response of the structure in several configurations and under typical pressure loading conditions of a Mars entry mission.
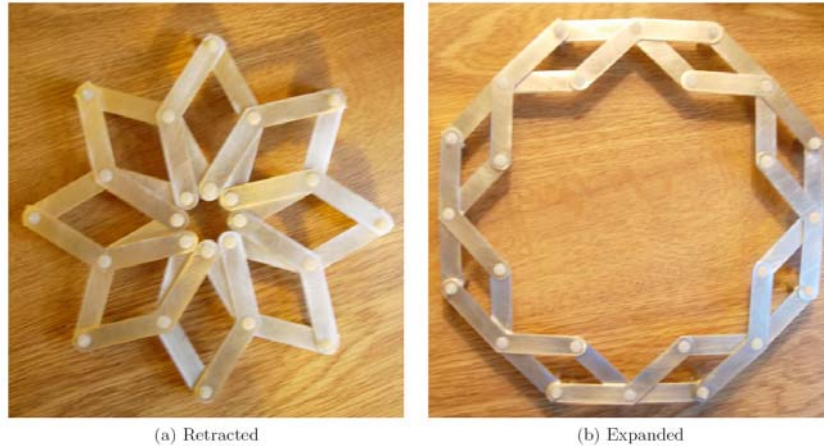
Figure 12. Foldable bar structure at (a) retracted and (b) expanded configuration.

A. Analysis Details

The dimensions and parameters for the model used in the simulation were chosen on the basis of the MSL mission[2] and are summarized in Table 1. The model is designed for average cone angles ranging from 60 deg to 70 deg; a cone angle of 67 deg in the undeformed state was chosen to approximately equalize the magnitude of the actuation forces in the two extreme configurations.

In the ABAQUS model, meridian ribs have been introduced under the valleys of the corrugated surface to provide attachment locations for the actuation mechanism. The ribs were modeled using eight-node full integration solid elements C3D8, while the surface was modeled using eight-node (SC8R) and six-node (SC6R) reduced integration continuum shell elements. The material was aluminum throughout, with linearly elastic and isotropic properties.

The analysis consisted of two steps. In the first step, the corrugated shell was deformed to achieve the required cone angle without any external loading. This was done by defining a contact pair between each rigid pin and the hole in the corresponding rib using the option 'CONTACT PAIR' and prescribing a radial displacement boundary condition on the pin. A uniformly distributed pressure simulating the aerodynamic loading was then applied on the front surface of the model in the second step. A pressure value of 10 kPa, corresponding to the maximum deceleration point in the trajectory, was used. Two translational and three rotational degrees of freedom on the pins were fixed while all other degrees of freedom were left unrestrained throughout the analysis. The simulation was carried out for several different configurations where the cone angles varied from 60 deg to 70 deg with 67 deg at the undeformed state. Both analysis steps were geometrically non-linear. Since the geometry is 12-fold rotationally symmetric and the pressure load is uniform, the analysis was carried out on a substructure that is a 1/12 section of the whole structure.

Table I. Corrugated shell model parameters

Diameter (m)	4.50
Bluntness Ratio	0.17
Nose Radius (m)	0.985
Number of Corrugations	12
Corrugation Amplitude (deg)	3.18
Shell Thickness (mm)	3.0

B. Results

The distribution of hoop and meridional stress resulting from the geometry change only is presented in Fig. 13. The corrugation amplitude increases when the cone angle is reduced and vice-versa, while the spherical cap experiences little deformation. This is because of the relatively higher stiffness of the spherical cap than the corrugated conical surface. The hoop stress induced by this deformation is a direct result of the change in corrugation amplitude. These changes in corrugation amplitude are associated with bending hoop stresses throughout the shell. The hoop stress is highest near the transition between the spherical cap and the corrugated cone and decreases along the meridian because the change in hoop curvature is the most significant when r is small. The meridional stress reaches a similar peak value, but is more localized near the transition.

Figure 14 shows the distribution of hoop and meridional stress under uniform pressure for the two configurations. Uniform pressure distribution essentially corresponds to the situation where a sphere-cone decelerator is flying at a zero angle of attack. In a lifting entry, the pressure distribution will be dependent on the angle of attack according to Eq. (7). For the proposed corrugated shell concept, the corrugations also change the local surface normal direction and therefore a numerical procedure will need to be employed to calculate more accurately the pressure distribution on the structure for different flight conditions. Figure 15 shows the radial actuation force at one connection point between the shell and the actuation mechanism, required to obtain the desired range of cone angles for the case of zero pressure and the case of uniform pressure. With zero pressure load, the actuation force varies nonlinearly with change in cone angle because of geometric nonlinearity in the deformation process. As the cone angle increases from the undeformed state, the corrugations flatten and so the structure increases its stiffness against this actuation mode. Conversely, when the cone angle reduces the corrugations amplify, and so the structure becomes softer. The uniform pressure load tends to expand the diameter of the outer rim, which induces an increase in the radial reaction force.
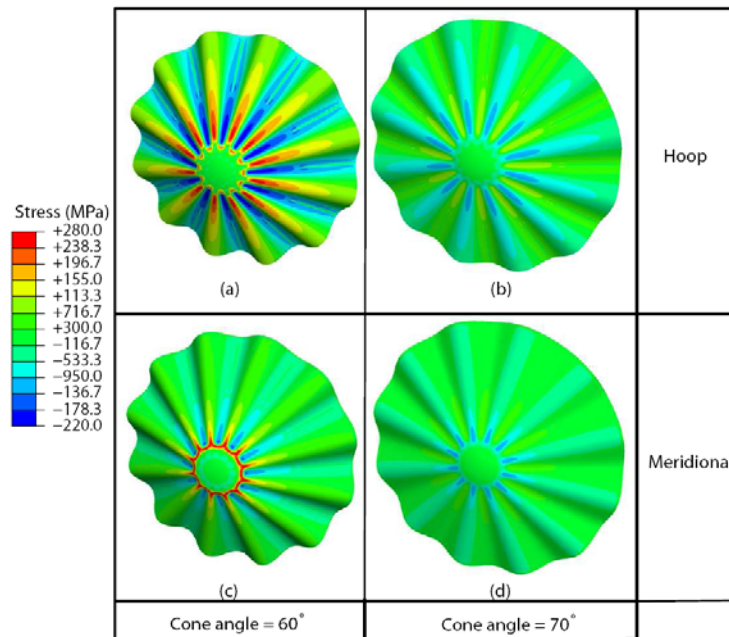

Figure 13. Distribution of stresses due to geometry change only for average cone angles 60 deg and 70 deg.
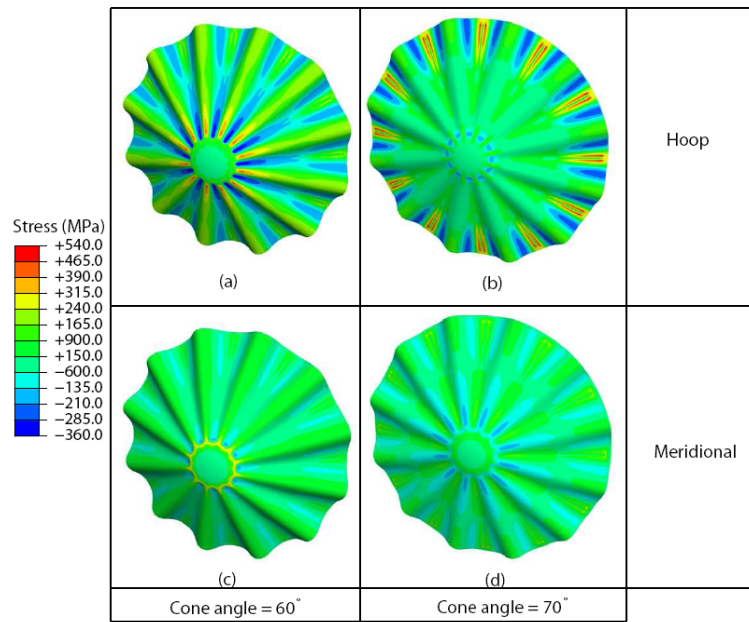
American Institute of Aeronautics and Astronautics

Figure 14. Distribution of stresses due to geometry change and uniform pressure for average cone angles 60 deg and 70 deg.
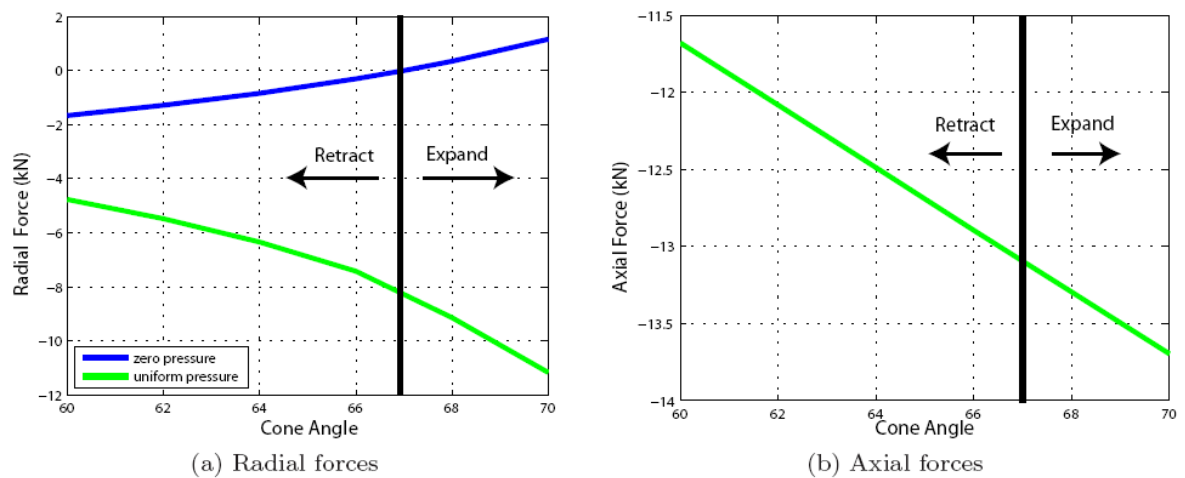

Figure 15. Reaction forces for cone angle variation in corrugated shell model.

VI.   Guidance Laws

This section describes three guidance laws based on the concept of dynamic inversion[15]. Similar guidance laws have been applied in related studies [12,13,14].

A. Guidance Laws for Constant Drag Tracking

Using the expression for the drag force given above, the drag tracking guidance is based on defining the error

$$e_D = D - D_{ref} \tag{10}$$

The error is reduced by imposing an exponentially stable error dynamics in the form [15]:

$$\ddot{e}_D + 2\zeta_D \omega_D \dot{e}_D + \omega_D^2 e_D = 0 \tag{11}$$

where $\omega\omega_D$ and $\zeta\zeta_D$ are the natural frequency and damping ratio of this second order system.
In terms of the drag force, this expression becomes:

$$\ddot{D} + 2\zeta_D \omega_D \dot{D} + \omega_D^2 \left(D - D_{ref} \right) = 0 \tag{12}$$

Where

$$\dot{D} = -2c_1 \rho V \frac{D}{m} - 2c_1 \rho V g \sin\gamma - c_1 \beta_a \rho V^3 \sin\gamma \tag{13}$$

$$\ddot{D} = -a_1 \dot{\gamma} - b_1$$

$$a_1 = c_1 \rho V \cos\gamma (2g + \beta_a V^2)$$

$$b_1 = 2c_1 \left(\dot{\rho} V \frac{D}{m} + \rho \dot{V} \frac{D}{m} + \rho V \frac{\dot{D}}{m} \right) + 2c_1 g \sin\gamma \left(\dot{\rho} V + \rho \dot{V} \right) + c_1 V^2 \beta_a \sin\gamma \left(\dot{\rho} V + 3\rho \dot{V} \right)$$

Consequently, the commanded flight-path-angle becomes:

$$\dot{\gamma}_{Cmd} = \frac{2\zeta_D \omega_D \dot{D} + \omega_D^2 \left(D - D_{ref} \right) - b_1}{a_1} \tag{14}$$

And the commanded bank angle becomes, from the longitudinal equation of motion, neglecting the small Earth curvature terms:

$$\sigma_{Cmd} = \cos^{-1} \left[\frac{V\dot{\gamma}_{Cmd} + \left(g - \frac{V^2}{r} \right) \cos\gamma}{L/m} \right] \tag{15}$$

B. Guidance Laws for Constant Heat-Rate Tracking

Using the expression for the convective heat flux input given above, the heat-rate tracking guidance is based on defining the error

$$e_Q = \dot{Q} - \dot{Q}_{ref} \tag{16}$$

The error is reduced by imposing an exponentially stable error dynamics in the form:

$$\ddot{e}_Q + 2\zeta_Q \omega_Q \dot{e}_Q + \omega_Q^2 e_Q = 0 \tag{17}$$

where ω_Q and ζ_Q are the natural frequency and damping ratio of this second order system.
In terms of the heat flux, we have:

$$e_Q = c_1 \rho^{\frac{1}{2}} V^3 - \dot{Q}_{ref}$$

$$\dot{e}_Q = -c_1 \rho^{\frac{1}{2}} V^2 \left(3g \sin\gamma + 3\frac{D}{m} + \frac{\beta_a}{2} V^2 \sin\gamma \right) \tag{18}$$

$$\ddot{e}_Q = a_2 + b_2 \dot{\gamma}_{Cmd}$$

Where:

$$b_2 = -c_1 \rho^{\frac{1}{2}} V \cos\gamma \left(3gV + \frac{\beta_a}{2} V^3 \right)$$

$$a_2 = c_1 \rho^{\frac{1}{2}} V \left[\beta_a V^2 \sin\gamma \left(g \sin\gamma + \frac{D}{m} \right) + 3\frac{D}{m} \beta_a V^2 \sin\gamma + 6\frac{D}{m} \left(g \sin\gamma + \frac{D}{m} \right) \right] + \tag{19}$$

$$\rho^{\frac{1}{2}} \left(3g \sin\gamma + 3\frac{D}{m} + \frac{\beta_a}{2} V^2 \sin\gamma \right) \left(2c_1 V \sin\gamma + \frac{DV}{m} + \frac{\beta_a}{2} V^3 \sin\gamma \right)$$

Consequently, the commanded flight-path-angle becomes:

$$\dot{\gamma}_{Cmd} = -\frac{2\zeta_Q \omega_Q \ddot{Q} + \omega_Q^2 \left(\dot{Q} - \dot{Q}_{ref} \right) + a_2}{b_2} \tag{20}$$

And the commanded bank angle becomes, from the longitudinal equation of motion:

$$\sigma_{Cmd} = \cos^{-1} \left[\frac{V\dot{\gamma}_{Cmd} + \left(g - \frac{V^2}{r} \right) \cos\gamma}{L/m} \right] \tag{21}$$

C. Guidance Laws for Constant Acceleration Load Tracking

Introducing the factor $u = \dfrac{L}{D}$, the aerodynamic acceleration load can be written as:

$$a_n = \frac{\left(D^2 + L^2 \right)^{1/2}}{m} = \frac{D}{m} \left(1 + u^2 \right)^{1/2} \tag{22}$$

The acceleration-load tracking guidance is then based on defining the error

$$e_a = a_n - \left(a_n\right)_{ref} \tag{23}$$

The error is reduced by imposing an exponentially stable error dynamics in the form:

$$\ddot{e}_a + 2\zeta_a \omega_a \dot{e}_a + \omega_a^2 e_a = 0 \tag{24}$$

where ω_a and ζ_a are the natural frequency and damping ratio of this second order system. We obtain:

$$e_a = \frac{D}{m}\left(1+u^2\right)^{1/2} - \left(a_n\right)_{ref}$$

$$\dot{e}_a = \frac{\dot{D}}{m}\left(1+u^2\right)^{1/2} + \frac{L}{m}\dot{u}\left(1+u^2\right)^{-1/2} \tag{25}$$

$$\ddot{e}_a = y_1 + x_1 \dot{\gamma}_{Cmd}$$

where:

$$\dot{D} = \frac{C_D S}{2}\left[-\beta_a \rho V^3 \sin\gamma - 2\rho V\left(g\sin\gamma + \frac{D}{m}\right)\right]$$

$$\dot{L} = \frac{C_L S}{2}\left[-\beta_a \rho V^3 \sin\gamma - 2\rho V\left(g\sin\gamma + \frac{D}{m}\right)\right]$$

$$\dot{\rho} = -\beta_a \rho V \sin\gamma$$

$$\dot{u} = \frac{\dot{L}D - \dot{D}L}{D^2} \tag{26}$$

$$\ddot{D} = m_1 \dot{\gamma} + n_1$$

$$\ddot{L} = p_1 \dot{\gamma} + q_1$$

$$\ddot{u} = r_1 \dot{\gamma} + t_1$$

$$r_1 = \frac{p_1 D - m_1 L}{D^2}$$

$$t_1 = \frac{\left(q_1 D - m_1 L\right) - \dot{L}\dot{D} - \dot{D}\dot{u}D + \dot{D}^2 u}{D^2}$$

$$m_1 = -\frac{C_D S}{2}\rho\cos\gamma\left(\beta_a V^3 + 2Vg\right)$$

$$n_1 = \frac{C_D S}{2}\left[-\beta_a \dot{\rho} V^3 \sin\gamma - 3\beta_a \rho \dot{V} V^2 \sin\gamma - 2\rho V\frac{D}{m} - 2\left(\dot{\rho}V + \rho\dot{V}\right)\left(g\sin\gamma + \frac{D}{m}\right)\right]$$

$$p_1 = -\frac{C_L S}{2}\rho\cos\gamma\left(\beta_a V^3 + 2Vg\right)$$

$$q_1 = \frac{C_L S}{2}\left[-\beta_a \dot{\rho} V^3 \sin\gamma - 3\beta_a \rho \dot{V} V^2 \sin\gamma - 2\rho V\frac{D}{m} - 2\left(\dot{\rho}V + \rho\dot{V}\right)\left(g\sin\gamma + \frac{D}{m}\right)\right]$$

$$x_1 = \frac{m_1}{m}\left(1+u^2\right)^{1/2} + \frac{L}{m}r_1\left(1+u^2\right)^{-1/2}$$

$$y_1 = \frac{n_1}{m}\left(1+u^2\right)^{1/2} + \frac{\dot{D}u\dot{u}}{m}\left(1+u^2\right)^{-1/2} + \frac{\dot{L}\dot{u}}{m}\left(1+u^2\right)^{-1/2} + \frac{L}{m}t_1\left(1+u^2\right)^{-1/2} - \frac{Lu\dot{u}^2}{m}\left(1+u^2\right)^{-3/2} \tag{27}$$

Consequently, the commanded flight-path-angle becomes:

$$\dot{\gamma}_{Cmd} = -\frac{2\zeta_a \omega_a \dot{e}_a + \omega_Q^2 e_a + y_1}{x_1} \tag{28}$$

And the commanded u becomes, from the longitudinal equation of motion:

$$u_{Cmd} = \left(\frac{L}{D}\right)_{Cmd} = \frac{m}{D}\left[V\dot{\gamma}_{Cmd} + \left(g - \frac{V^2}{r}\right)\cos\gamma\right] \tag{29}$$

VII. Trajectory Analysis and Results

A trajectory study has been conducted, which makes use of the variable geometry concepts described above. Figure 16 and Figure 17 show results of the simulation where the cone angle is increased 10 degrees in a step of 60 seconds (case 1). Figure 18 and Figure 19 show results of a second simulation study (case 2) where the cone angle is actuated when the following three conditions are verified: resultant acceleration load > 10 m/s^2, rate of change of temperature > 10.0 K/s, and temperature > 500.0 K. These results indicate that small changes in the geometry of the low L/D configuration can effectively influence the main dynamic variables that are required for maneuvering the vehicle, namely the drag force, acceleration load, and heat flux. More detailed analysis of this interaction are subject of future work.

VIII. Conclusion

The results presented in this paper apply to a generic vehicle entering a planetary atmosphere which makes use of a variable geometry change to modulate the heat, drag, and acceleration loads. Innovative structural concepts are presented that are very promising to implement a variable geometry aerodynamic shape. A structural analysis of these proposed structural configuration shows that the stress levels are tolerable during entry.

Two structural concepts for implementing the cone angle variation, namely a segmented shell and a corrugated shell, have been presented. Small proof-of-concept prototypes have shown that a change of cone angle in the range 60∘ to 70∘ is achievable with both concepts. The structural performance of the full scale (4.5 m diameter) corrugated shell decelerator concept has been analyzed assuming a uniformly distributed pressure loading of 10 kPa. Assuming an aluminum shell with a uniform thickness of 3.0 mm, a peak stress of 540 MPa has been predicted near the transition between the spherical cap and the corrugated conical surface when the cone angle is reduced from 67 deg to 60 deg. The same stress magnitude has been found when the cone angle is increased from 67 deg to 70 deg, but the peak stress occurs near the outer rim of the shell. A total radial actuation force of 134 kN is needed to maintain the corrugated shell at a cone angle of 70 deg. These preliminary results indicate the broad feasibility of the proposed scheme, although of course it will be necessary to refine the proposed design to ensure that the peak stresses are within acceptable limits for a specific material. It is possible that a multiparameter optimization approach will be necessary to fully explore the potential of the proposed solution. Since the shape of corrugated shell deviates from the conventional sphere-cone decelerator, the variation of aerodynamic characteristics with cone angle obtained is an approximation to that of the corrugated shell decelerator. A more precise numerical computation of the pressure distribution on the corrugated shell surface using panel method is currently underway. This numerical procedure will be incorporated into the trajectory simulation and the structural analysis. Scaled prototypes for both concepts were fabricated. They have demonstrated that continuous variation in cone angle is achievable. Further work will also include tuning the current corrugated shell geometry using an energy-based optimization approach to minimize stress and actuation force, and exploring trajectory modulation with decelerators undergoing asymmetric variation in geometry.

Variations in cone angle for a decelerator with sphere-cone geometry have the effect of altering the trim angle of attack and the corresponding lift-to-drag ratio and ballistic coefficients during flight. This capability enables trajectory optimization with fewer aerodynamic constraints. The analytical expressions of the longitudinal

American Institute of Aeronautics and Astronautics

aerodynamic coefficients were derived, and guidance laws that track reference heat flux, drag, and aerodynamic acceleration loads are also proposed. These guidance laws, based on dynamic inversion, have been tested in an integrated simulation environment, and the results indicate that use of variable geometry is feasible to track specific profiles of dynamic load conditions during reentry.
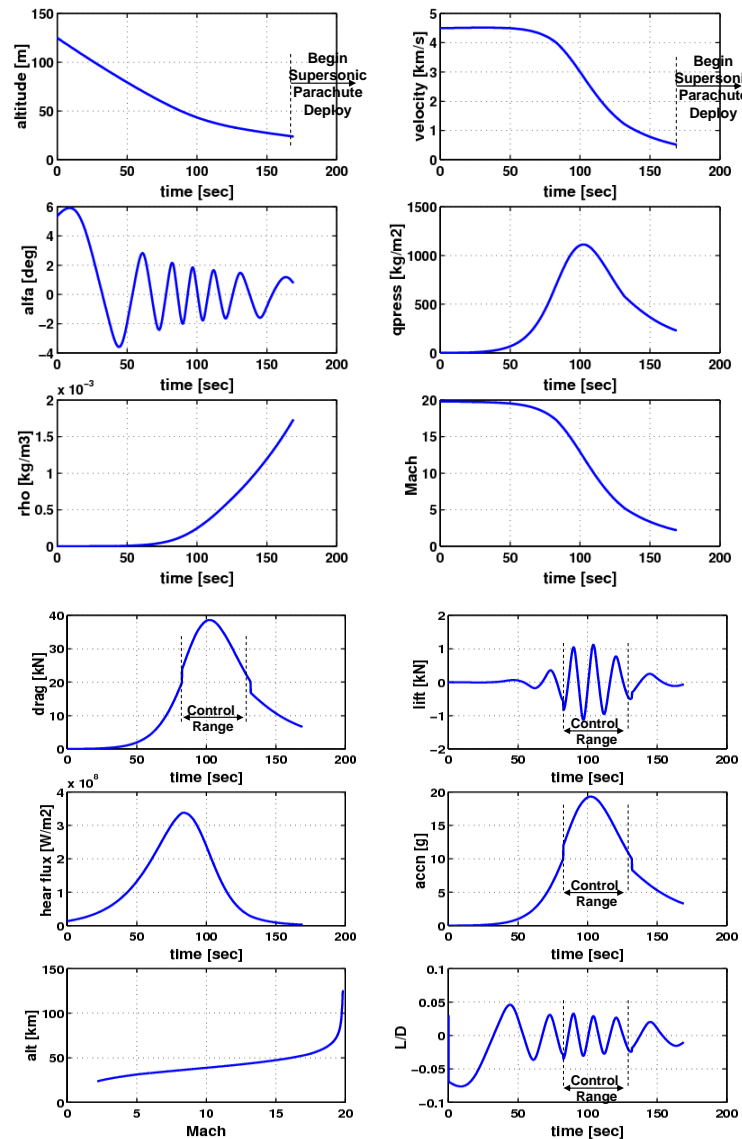

Figure 16. Representative simulation results for case 1 – alfa = angle-of-attack; qpress = dynamic pressure, rho= air density; accn = magnitude of acceleration; alt = altitude.

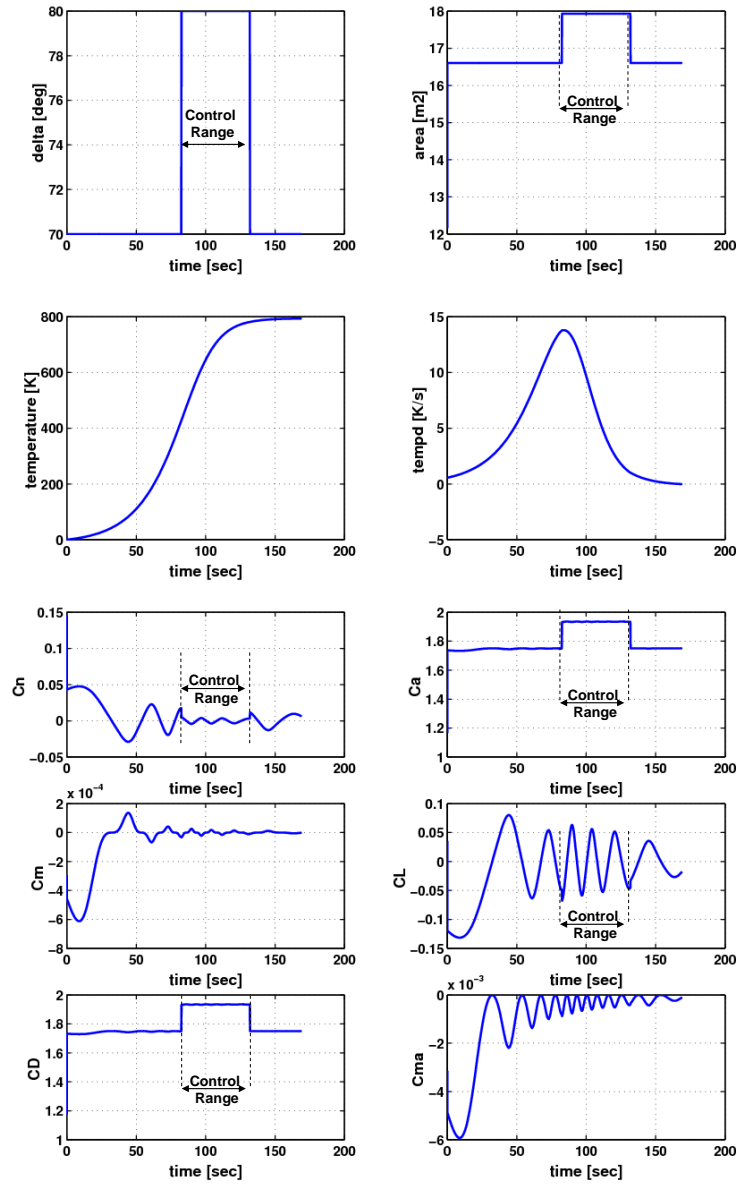American Institute of Aeronautics and Astronautics

Figure 17. Representative simulation results for case 1 – delta = sphere-cone angle; area = vehicle exposed area; tempd = temperature time rate of change; Cma = $\partial C_m / \partial \alpha$.
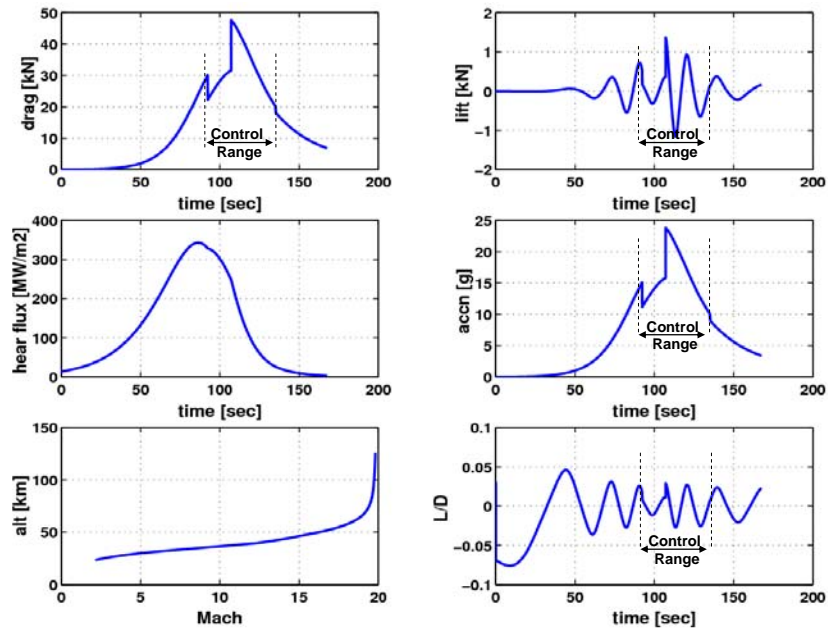
American Institute of Aeronautics and Astronautics

Figure 18. Representative simulation results for case 2 – alfa = angle-of-attack; qpress = dynamic pressure, rho= air density; accn = magnitude of acceleration; alt = altitude.
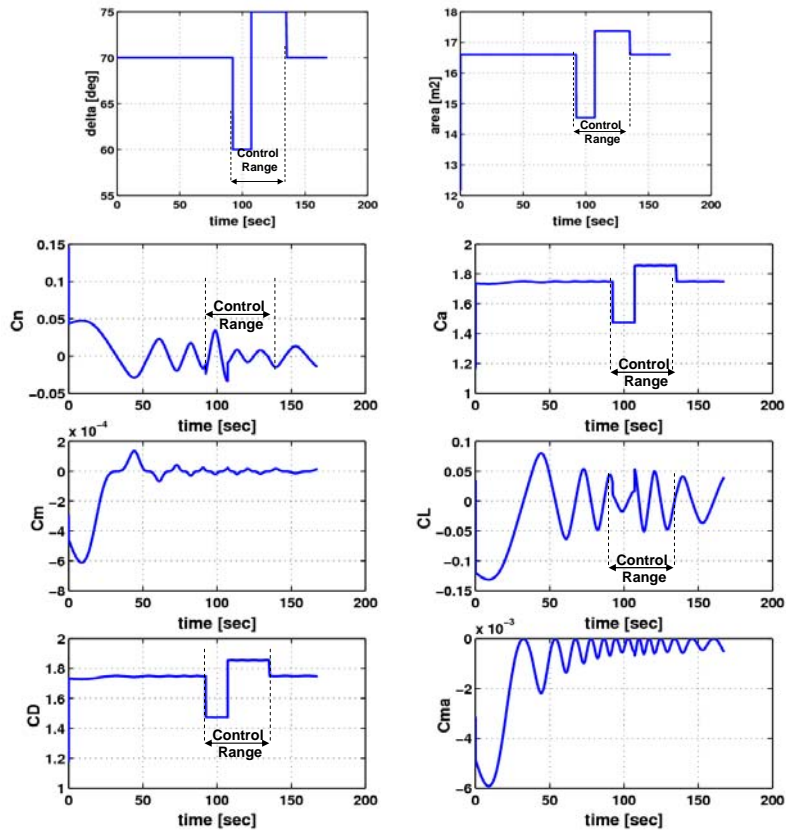

Figure 19. Representative simulation results for case 2 – delta = sphere-cone angle; area = vehicle exposed area; tempd = temperature time rate of change; Cma = $\partial C_m / \partial \alpha$.

American Institute of Aeronautics and Astronautics

Acknowledgments

References

1. Braun, R.D., and Manning, R.M., *Mars Exploration Entry, Descent and Landing Challenges*, IEEEAC Paper 0076, Dec. 2005.

2. Way, D.W., Powell, R.W., Chen, A., Steltzner, A.D., Martin, A.M.S., Burkhart, P.D., and Mendeck, G.F., *Mars Science Laboratory: Entry, Descent, and Landing System Performance*, IEEEAC Paper 11467, Feb. 2006

3. Lockwood, M.K., Powell, R.W., Sutton, K., Prabhu, R.K., Graves, C.A., Epp, C.D., and Carman, G.L., *Entry Configurations and Performance Comparisons for the Mars Smart Lander*, Journal of Spacecraft and Rockets, Vol. 43, No.2, 2006, pp. 258-269.

4. Regan, F.J., and Anandakrishnan, S.M., "Re-Entry Vehicle Particle Mechanics," *Dynamics of Atmospheric Re-Entry*, edited by J.S. Przemieniecki, AIAA Education Serise, AIAA, Washington D.C., 1993, pp. 179-207.

5. Regan, F.J., "Flowfield Description," *Re-Entry Vehicle Dynamics*, edited by J.S. Przemieniecki, AIAA Education Serise, AIAA, Washington D.C., 1984, pp. 219-234.

6. Edquist, K.T., Hollis, B.R., Dyakonov, A.A., Laub, B., Wright, M.J., Rivellini, T.P., Slimko, E.M., Willcockson, W.H., *Mars Science Laboratory Entry Capsule Aerothermodynamics and Thermal Protection System*, IEEEAC Paper 1423, Jan. 2007.

7. Kustas, F.M., Rawal, S.P., Willcockson, W.H., Edquist, C.T., Thornton, J.M., *Evaluation of High-Temperature Multi-layer Insulation for Inflatable Ballute*, Journal of Spacecraft and Rockets, Vol. 38, No.4, 2001, pp. 630-631.

8. SIMULIA, ABAQUS/STANDARD Version 6.7, Providence, RI.

9. Stereolithography Product Data Sheets, DSM Somos, Elgin, ILL.

10. You, Z., and Pellegrino, S., *Foldable Bar Structures*, International Journal of Solids and Structures, Vol. 34, No.15, 1997, pp. 1825-1847.

11. Ashley, H.: *Engineering Analysis of Flight Vehicles*, Dover Publications, 1992.

12. Quadrelli, B.M.: *A Novel Approach to Planetary Precision Landing using Parafoils*, presented at the 15th AAS Space Flight Mechanics Meeting, Copper Mountain, CO, 23-27 January 2005.

13. Smith R.S., Mease K.D., Bayard D.S. & Farless D.L., *Aeromaneuvering in the Martian Atmosphere: Simulation-Based Analyses*, AIAA Journal of Spacecraft and Rockets, Vol. 37, No. 1, pp. 139–142, 2000.

14. Smith R.S., Boussalis D. and Hadaegh F., *Closed-Loop Aeromaneuvering for a Mars Precision Landing*, NASA URC Tech. Conf., Albuquerque, NM, pp. 942–947, Feb., 1997.

15. Hanson, J.M., Couglin, D. J., Dukeman, G.A., Mulqueen, J.A., McCarter, J.W.: *Ascent, Transition, Entry, and Abort Guidance Algorithm Design for the X-33 Vehicle*, AIAA paper 97-4409.

16. Vinh, Busemann, Culp: *Hypersonic and Planetary Entry Flight Mechanics*, Ann Arbor, University of Michigan Press, 1980.

17. Gallais, P.: *Atmospheric Re-entry Vehicle Mechanics*, Springer, 2007.